

Scanning Camera for Continuous-Wave Acoustic Holography

Hillary W. Gao, Kimberly I. Mishra, Annemarie Winters, Sidney Wolin, and David G. Grier*

Department of Physics and Center for Soft Matter Research,

New York University, New York, NY 10003, USA

(Dated: August 9, 2018)

We present a system for measuring the amplitude and phase profiles of the pressure field of a harmonic acoustic wave with the goal of reconstructing the volumetric sound field. Unlike optical holograms that cannot be reconstructed exactly because of the inverse problem, acoustic holograms are completely specified in the recording plane. We demonstrate volumetric reconstructions of simple arrangements of objects using the Rayleigh-Sommerfeld diffraction integral, and introduce a technique to analyze the dynamic properties of insonated objects.

Most technologies for acoustic imaging use the temporal and spectral characteristics of acoustic pulses to map interfaces between distinct phases. This is the basis for sonar [1], and medical and industrial ultrasonography [2]. Imaging continuous-wave sound fields is useful for industrial and environmental noise analysis, particularly for source localization [3]. Substantially less attention has been paid to visualizing the amplitude and phase profiles of sound fields for their own sakes, with most effort being focused on visualizing the near-field acoustic radiation emitted by localized sources, a technique known as near-field acoustic holography (NAH) [4–6]. The advent of acoustic manipulation in holographically structured sound fields [7–11] creates a need for effective sound-field visualization. Here, we demonstrate a scanning acoustic camera that combines lockin detection with a polarograph for flexible large-area scanning to accurately record the wavefront structure of acoustic travelling waves. Borrowing techniques from optical holography, we use Rayleigh-Sommerfeld back-propagation [12] to reconstruct the three-dimensional sound field associated with the complex pressure field in the measurement plane. These reconstructions, in turn, provide insights into the dynamical properties of objects immersed in the acoustic field.

HOLOGRAPHY

A harmonic traveling wave at frequency ω can be described by a complex-valued wave function,

$$\psi(\mathbf{r}, t) = u(\mathbf{r}) e^{i\varphi(\mathbf{r})} e^{-i\omega t}, \quad (1)$$

that is characterized by real-valued amplitude and phase profiles, $u(\mathbf{r})$ and $\varphi(\mathbf{r})$, respectively. Eq. (1) can be generalized for vector fields by incorporating separate amplitude and phase profiles for each of the Cartesian coordinates. The field propagates according to the wave equation,

$$\nabla^2 \psi = k^2 \psi, \quad (2)$$

where the wave number k is the magnitude of the local wave vector,

$$\mathbf{k}(\mathbf{r}) = \nabla \varphi(\mathbf{r}). \quad (3)$$

A hologram is produced by illuminating an object with an incident wave, $\psi_0(\mathbf{r}, t)$, whose amplitude and phase profiles are $u_0(\mathbf{r})$ and $\varphi_0(\mathbf{r})$, respectively. The object scatters some of that wave to produce $\psi_s(\mathbf{r}, t)$, which propagates to the imaging plane. In-line holography uses the remainder of the incident field as a reference wave that interferes with the scattered field to produce a superposition

$$\psi(\mathbf{r}, t) = \psi_0(\mathbf{r}, t) + \psi_s(\mathbf{r}, t) \quad (4)$$

whose properties are recorded. The wave equation then can be used to numerically reconstruct the three-dimensional field from its value in the plane. In this way, numerical back-propagation can provide information about the object's position relative to the recording plane as well as its size, shape and properties. The nature of the recording determines how much information can be recovered.

Optical holography: Intensity holograms

Optical cameras record the intensity of the field in the plane, and so discard all of the information about the wave's direction of propagation that is encoded in the phase. Interfering the scattered wave with a reference field yields an intensity distribution,

$$I(\mathbf{r}) = |\psi(\mathbf{r}, t)|^2 \quad (5a)$$

$$= \left| u_0(\mathbf{r}) e^{i\varphi_0(\mathbf{r})} + u_s(\mathbf{r}) e^{i\varphi_s(\mathbf{r})} \right|^2, \quad (5b)$$

that blends information about both the amplitude and the phase of the scattered wave into a single scalar field.

The properties of the scattered field can be interpreted most easily if the incident field can be modeled as a unit-amplitude plane wave,

$$\psi_0(\mathbf{r}, t) \approx e^{ikz} e^{-i\omega t}, \quad (6a)$$

in which case,

$$I(\mathbf{r}) \approx \left| 1 + u_s(\mathbf{r}) e^{i\varphi_s(\mathbf{r})} \right|^2. \quad (6b)$$

If, furthermore, the scattering process may be modeled with a transfer function,

$$\psi_s(\mathbf{r}) = T(\mathbf{r} - \mathbf{r}_s) \psi_0(\mathbf{r}_s), \quad (6c)$$

then $I(\mathbf{r})$ can be used to estimate parameters of $T(\mathbf{r})$, including the position and properties of the scatterer.

This model has proved useful for interpreting in-line holograms of micrometer-scale colloidal particles [13]. Fitting to Eq. (6) can locate a colloidal sphere in three dimensions with nanometer precision [14, 15]. The same fit yields estimates for the sphere's diameter and refractive index to within a part per thousand [15]. Generalizations of this method [16] work comparably well for tracking clusters of particles [17–19].

Rayleigh-Sommerfeld back propagation

The success of fitting methods is based on *a priori* knowledge of the nature of the scatterer, which is encoded in the transfer function, $T(\mathbf{r})$. In instances where such knowledge is not available, optical holograms also can be used as a basis for reconstructing the scattered field, $\psi_s(\mathbf{r}, t)$, in three dimensions. This reconstruction can serve as a proxy for the structure of the sample.

One particularly effective reconstruction method [12, 20] is based on the Rayleigh-Sommerfeld diffraction integral [21]. The field, $\psi(x, y, 0, t)$ in the imaging plane, $z = 0$, propagates to point \mathbf{r} in plane z as [21]

$$\psi(\mathbf{r}, t) = \psi(x, y, 0, t) \otimes h_z(x, y), \quad (7a)$$

where

$$h_z(x, y) = \frac{1}{2\pi} \frac{d}{dz} \frac{e^{ikr}}{r}. \quad (7b)$$

is the Rayleigh-Sommerfeld propagator. The convolution in Eq. (7) is most easily computed with the Fourier convolution theorem using the Fourier transform of the propagator,

$$H_z(\mathbf{q}) = e^{-iz\sqrt{k^2 - q^2}}. \quad (8)$$

Equation (7) can be used to numerically propagate a measured wave back to its source, thereby reconstructing the three-dimensional field responsible for the recorded pattern.

Acoustic holography: Complex holograms

Early implementations of acoustic holography resembled optical holography in recording the intensity of

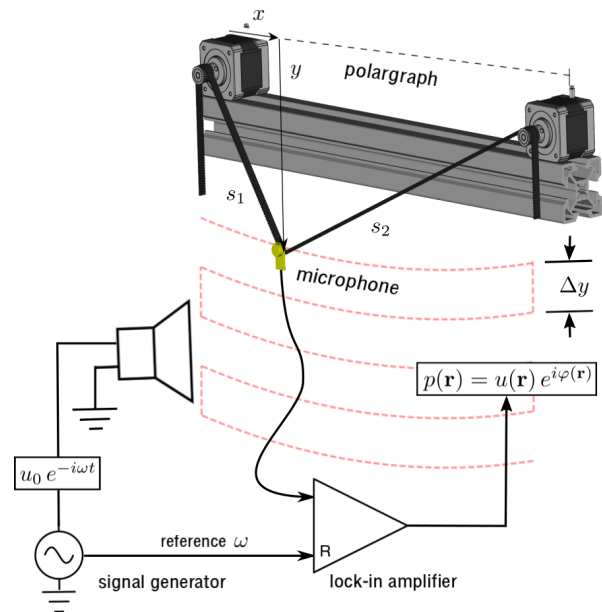


FIG. 1. (color online) Schematic representation of the scanning acoustic camera. A polargraph composed of two stepping motors and a timing belt translates a microphone across the field of view in a serpentine pattern. A harmonic sound field is created by an audio speaker driven by a signal generator. The signal detected by the microphone is analyzed by a lock-in amplifier to obtain the amplitude $u(\mathbf{r})$ and phase $\varphi(\mathbf{r})$ of the sound's pressure field at each position $\mathbf{r} = (x, y)$.

the sound field [22]. Sound waves of modest intensity, however, are fully characterized by a scalar pressure field, $p(\mathbf{r}, t)$, whose amplitude and phase can be measured directly. In that case, Rayleigh-Sommerfeld back-propagation can be used to reconstruct the complex sound field with an accuracy that is limited by instrumental noise and by the size of the recording area. For appropriate systems, the transfer-function model can be used to obtain information about scatterers in the field.

Whereas optical holography benefits from highly developed camera technology, implementations of quantitative acoustic holography must confront a lack of suitable area detectors for sound waves. Commercial acoustic transducer arrays typically include no more than a few dozen elements. Conventional area scanners yield excellent results over small areas [10] but become prohibitively expensive for large-area scans. We therefore introduce flexible and cost-effective techniques for recording complex-valued acoustic holograms.

SCANNING ACOUSTIC CAMERA

Figure 1 depicts our implementation of a scanning acoustic camera for holographic imaging. A signal generator (Stanford Research Systems DS345) drives an audio speaker at a desired frequency ω . The resulting sound

wave propagates to a microphone whose output is analyzed by a dual-phase lock-in amplifier (Stanford Research Systems SR830) referenced to the signal generator. Our reference implementation operates at 8 kHz, which corresponds to a wavelength of 42.5 mm.

The lock-in amplifier records the amplitude and phase of the pressure field at the microphone's position. We translate the microphone across the x - y plane using a flexible low-cost two-dimensional scanner known as a polargraph that initially was developed for art installations [23]. Correlating the output of the lock-in amplifier with the position of the polargraph yields a map of the complex pressure field in the plane.

Polargraph for flexible wide-area scanning

The polargraph consists of two stepper motors (Nema 17, 200 steps/rev) with toothed pulleys (16 tooth, GT2, 7.5 mm diameter) that control the movement of a flexible GT2 timing belt, as indicated in Fig. 1. The acoustic camera's microphone (KY0030 high-sensitivity sound module) is mounted on a laser-cut support that hangs under gravity from the middle of the timing belt. The motors' rotations determine the lengths, $s_1(t)$ and $s_2(t)$ of the two chords of timing belt at time t , and therefore the position of the microphone, $\mathbf{r}(t)$. If the motors are separated by distance L and the microphone initially is located at height y_0 below their midpoint, then

$$\mathbf{r}(t) = x(t) \hat{x} + y(t) \hat{y}, \quad \text{where} \quad (9a)$$

$$x(t) = \frac{s_1^2 - s_2^2}{2L} \quad \text{and} \quad (9b)$$

$$y(t) = \sqrt{\frac{s_1^2 + s_2^2}{2} - \frac{L^2}{4} - x^2(t)} - y_0. \quad (9c)$$

In our implementation, $L = 1$ m and $y_0 = 10$ cm.

The stepper motors are controlled with an Arduino microcontroller that is addressed by software running on a conventional computer [24]. Smoothest operation is obtained by running the stepper motors at constant rates. This results in the microphone translating through a serpentine pattern, as indicated in Fig. 1. Horizontal sweeps of 0.6 m are separated by vertical steps of $\Delta y = 5$ mm, and the motors' step rates are configured to maintain a constant scan speed of 46.5 mm s^{-1} .

The polargraph is deployed by mounting the stepper motors at the upper corners of the area to be scanned. Our implementation has the motors mounted on a frame constructed from extruded 1-inch square aluminum T-slot stock, as indicated in Fig. 1. The scan area is limited by the length of the timing belt and by the requirement that both chords of the belt remain taut throughout the scan. This can be facilitated by adding weight to the microphone's mounting bracket or by adding a tensioning

cable. Mechanical vibrations during the scan are substantially smaller than the effective pixel size of the resulting acoustic holograms.

Lockin detection

While the polargraph scans the microphone across the field view, the lockin amplifier reports the amplitude and phase of the signal detected by the microphone. Setting the lockin's time constant to 30 ms effectively suppresses background noise yet is short enough to enable independent measurements at 0.1 s intervals. Given the translation speed, this corresponds to an effective spatial resolution of 4.65 ± 0.05 mm. The vertical separation, Δy , between horizontal sweeps is set accordingly. We report the relative amplitude of the instrument's response with full scale corresponding to roughly 1 Pa.

The amplifier's measurements of $u(t)$ and $\varphi(t)$ at time t are associated with the polargraph's position, $\mathbf{r}(t)$, that is computed with Eq. (9) at the same time. Because the lockin amplifier's readout is not synchronized to the polargraph's motion, this yields an irregularly gridded representation of the complex pressure field. We therefore resample $u(t)$ and $\varphi(t)$ onto a $128 \text{ pixel} \times 128 \text{ pixel}$ Cartesian grid (16384 effective pixels) with 4.90 ± 0.08 mm spacing using bilinear interpolation. This measurement grid is finer than the wavelength of sound and is substantially larger than can be achieved with currently available microphone arrays. The parameters selected here yield one complete measurement in about 25 min.

RESULTS

Holographic imaging

Figure 2(a) shows the amplitude and phase of the sound field reaching the recording plane when the speaker is located nearly 2 m away. The recording plane is normal to the direction of sound propagation and the walls of the $1.5 \text{ m} \times 1.5 \text{ m}$ experimental volume are lined with 2-inch wedge acoustic tiles to minimize reflections. Even so, off-axis reflections reach the measurement plane and interfere with the directly propagating sound field in the measurement plane. These interference features are particularly evident in the amplitude profile in Fig. 2(a) and appear in all of the results that we present.

The phase profile projected by the speaker is smoothly curved, which is expected for the diverging pressure field from a localized source. Taking the speed of sound in air to be $v = 340 \text{ m s}^{-1}$, the center of curvature of the phase profile is located 160 ± 10 cm away from the observation plane, which is consistent with the speaker's position. Because the lockin amplifier measures phase delay over a limited range, we present the phase modulo 2π . This

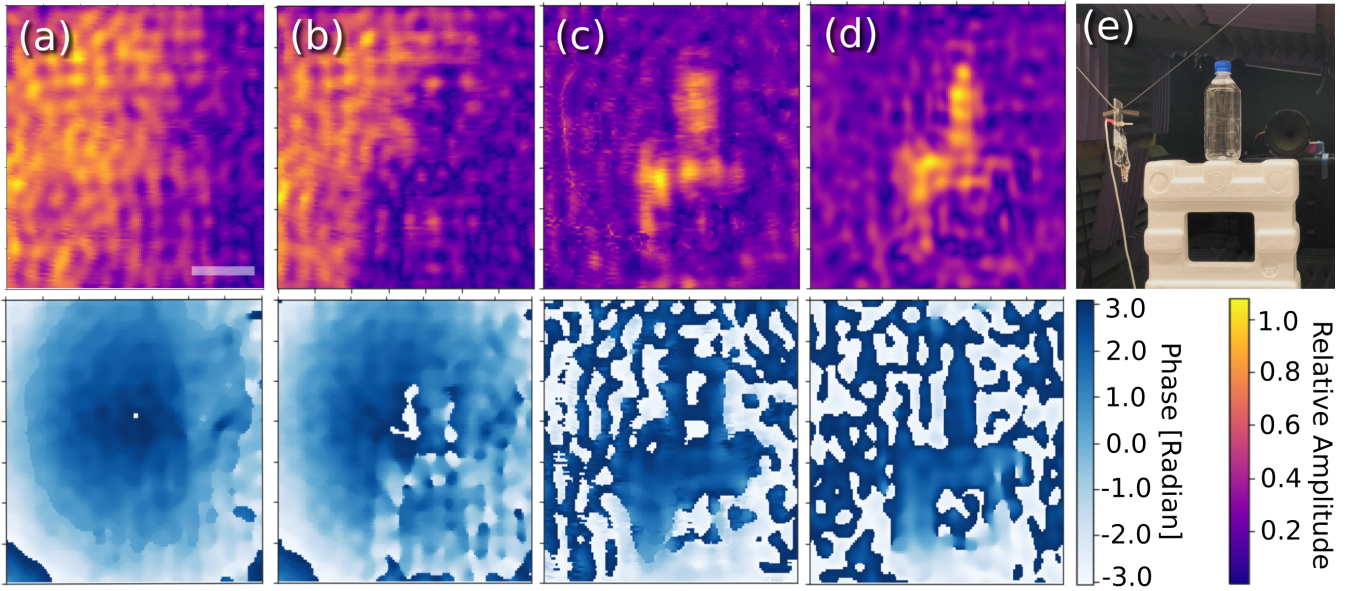


FIG. 2. (color online) Acoustic holography of objects in a sound field. (a) Amplitude (top) and phase (bottom) of the harmonic field at 8 kHz projected by a speaker nearly 2 m from the imaging plane. Scale bar corresponds to 15 cm. (b) The same field of view with scattering objects in the foreground. (c) Background-subtracted estimate for the scattered field in the imaging plane. (d) Refocused acoustic image obtained from (c) by Rayleigh-Sommerfeld back-propagation with Eq. (7). (e) Photograph of the scene recorded by the acoustic camera, including the camera's microphone.

causes abrupt transitions to appear in the rendering. We move these out of the field of view by shifting the lockin amplifier's phase response by $\Delta\varphi = 0.02^\circ$.

The complex pressure field, $p_0(\mathbf{r})$, serves as the background field for other holograms recorded by this instrument. Figure 2(b) shows the same field of view partially obstructed by a collection of objects, specifically a plastic bottle filled with water placed atop a styrofoam box. The objects appear as a shadow in the amplitude profile and as a pattern of discontinuities in the phase profile. Because the phase profile is wrapped into the range $0 \leq \varphi(\mathbf{r}) \leq 2\pi$, it cannot be used to measure the speed of sound within the objects. It does, however, provide enough information to reconstruct the three-dimensional sound field.

The complex pressure field in the imaging plane, $p(\mathbf{r}) = p_0(\mathbf{r}) + p_s(\mathbf{r})$, includes both the source field, $p_0(\mathbf{r})$, and the field scattered by the objects, $p_s(\mathbf{r})$. The difference $\Delta p(\mathbf{r}) = p(\mathbf{r}) - p_0(\mathbf{r})$ between the recorded hologram of the object and the previously recorded background pressure field is an estimate of the scattered field due to the object in the measurement plane. This is plotted in Fig. 2(c). The object's shadow appears bright in the amplitude distribution because it differs substantially from the background amplitude. The sign of this difference is encoded in the phase, which confirms that the object has reduced the sound level directly downstream.

Figure 2(d) shows the result of numerically reconstructing the field at a distance $z = 15.6$ cm behind the

recording plane. This effectively brings the object into focus without otherwise distorting its image. The result is consistent with a photograph of the scene, which is reproduced in Fig. 2(e).

Holographic characterization of dynamical properties

If the object scattering the incident wave is not substantially larger than the wavelength, the wave it scatters may be modeled as the incident wave in the scattering plane, $z = z_s$, modified by a complex transfer function:

$$p_s(x, y, z_s) = T(\mathbf{r}) p_0(x, y, z_s). \quad (10)$$

We estimate the transfer function by numerically back-propagating the incident wave to the scattering plane using Eq. (7), and using it to normalize the back-propagated scattered wave:

$$T(\mathbf{r}) = \frac{p(x, y, z_s)}{p_0(x, y, z_s)} - 1. \quad (11)$$

In the absence of any object, we expect $T(\mathbf{r}) = 0$.

Figure 3(a) shows the amplitude and phase of the transfer function, $T(\mathbf{r})$, of the sample from Fig. 2. As expected, the background amplitude of the computed transfer function has magnitude and phase near zero. The transfer function of a passive object should advance

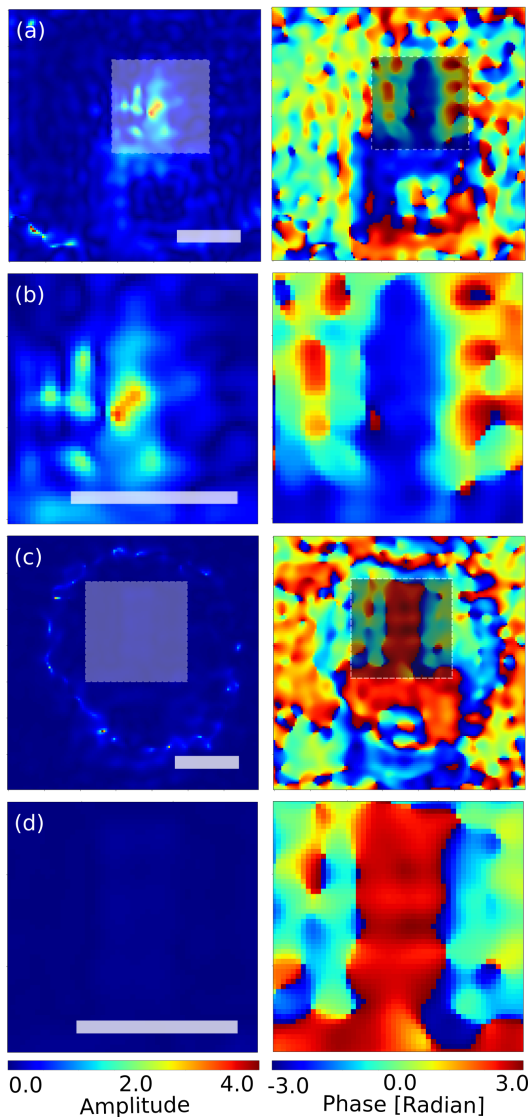


FIG. 3. (color online) Detecting and localizing mechanical resonances in insonated objects. (a) Amplitude (left) and phase (right) of the transfer function for the system in Fig. 2. Shaded boxes indicate the region of interest that is presented in (b). (c) Amplitude and phase of the transfer function for a system identical except with a similar-sized block of wood instead of a water bottle. Shaded boxes indicate the region of interest that is presented in (d). Scale bars correspond to 15 cm.

the phase of the incident wave while reducing its amplitude. We therefore expect $|T(\mathbf{r})| \leq 1$, with $T(\mathbf{r}) = -1$ corresponding to a perfect absorber. In fact, the water bottle's transfer function presents a well localized peak of magnitude 5 near one corner of the object. This can be seen more clearly in the expanded field of view in Fig. 3(b). The peak in the transfer function's amplitude is associated with a localized reversal of its phase. Most of the bottle's acoustic transfer function has phase $\arg T(\mathbf{r}) \approx -\pi$, which suggests that it is removing energy

from the field in those regions. The abrupt transition through $\arg T(\mathbf{r}) = 0$ to $\arg T(\mathbf{r}) = \pi$ near the bottle's left side is consistent with localized phase reversals in the region of the peak in $|T(\mathbf{r})|$. These observations suggest that this feature may be identified with a resonant mode of the water bottle that focuses acoustic energy.

To test this interpretation, we replace the water bottle with a comparably sized block of wood and repeat the measurement. The resulting transfer function is plotted in Fig. 3(c), with an expanded field of view in Fig. 3(d). The magnitude of the block's transfer function is no greater than 0.2 across the entire field of view in Fig. 3(d). The phase profile within the block similarly lacks any prominent features.

CONCLUSIONS

We have presented a scanning acoustic camera that can be deployed flexibly to record the amplitude and phase profiles of harmonic pressure fields over wide areas. We further have demonstrated the use of the Rayleigh-Sommerfeld propagator to back-propagate the measured acoustic hologram to reconstruct the three-dimensional sound field. This is useful for numerically refocusing a recorded image of an object immersed in the sound field. We have shown, furthermore, that numerical back propagation can be used to estimate an object's complex acoustic transfer function and thus to probe its dynamical properties at the driving frequency of the sound field. We demonstrate this by imaging a resonance in a container of water.

We anticipate that the acoustic imaging capabilities we have described will be useful for research groups deploying structured acoustic fields for communication, sensing and manipulation. In such cases, the scanning technique provides a cost-effective means to characterize the projected wave, even when it covers a very large area. The camera also is useful for creating images of scenes in continuous harmonic waves. Our implementation is deployed for imaging in transmission. Reflected and oblique imaging also should be possible. Numerically refocused acoustic imaging is particularly useful for remote imaging of dynamical properties.

While our implementation is based on lockin detection of harmonic waves, generalizations to broad-spectrum sources can be implemented with correlation-based detection. The scanned approach similarly should lend itself to imaging in noise[25], including imaging of dynamical properties.

This work was supported by the MRSEC program of the National Science Foundation through award number DMR-1420073.

* david.grier@nyu.edu

- [1] M. P. Hayes and P. T. Gough, "Synthetic aperture sonar: a review of current status," *IEEE J. Oceanic Engineering* **34**, 207–224 (2009).
- [2] A. Fenster and D. B. Downey, "3-D ultrasound imaging: A review," *IEEE Engin. Med. Bio. Mag.* **15**, 41–51 (1996).
- [3] X. Sheng and Y.-H. Hu, "Maximum likelihood multiple-source localization using acoustic energy measurements with wireless sensor networks," *IEEE Trans. Signal Processing* **53**, 44–53 (2005).
- [4] J. D. Maynard, E. G. Williams, and Y. Lee, "Nearfield acoustic holography: I. theory of generalized holography and the development of NAH," *J. Acoust. Soc. Am.* **78**, 1395–1413 (1985).
- [5] W. Veronesi and J. D. Maynard, "Nearfield acoustic holography (NAH) II. holographic reconstruction algorithms and computer implementation," *J. Acoust. Soc. Am.* **81**, 1307–1322 (1987).
- [6] E. G. Williams, *Fourier acoustics: sound radiation and nearfield acoustical holography* (Elsevier, 1999).
- [7] P. L. Marston, "Axial radiation force of a Bessel beam on a sphere and direction reversal of the force," *J. Acoust. Soc. Am.* **120**, 3518–3524 (2006).
- [8] P. Zhang, T. Li, J. Zhu, X. Zhu, S. Yang, Y. Wang, X. Yin, and X. Zhang, "Generation of acoustic self-bending and bottle beams by phase engineering," *Nature Commun.* **5**, 4316 (2014).
- [9] A. Marzo, S. A. Seah, B. W. Drinkwater, D. R. Sahoo, B. Long, and S. Subramanian, "Holographic acoustic elements for manipulation of levitated objects," *Nature Commun.* **6**, 8661 (2015).
- [10] K. Melde, A. G. Mark, T. Qiu, and P. Fischer, "Holograms for acoustics," *Nature* **537**, 518 (2016).
- [11] Y. Tian, Q. Wei, Y. Cheng, and X. Liu, "Acoustic holography based on composite metasurface with decoupled modulation of phase and amplitude," *Appl. Phys. Lett.* **110**, 191901 (2017).
- [12] S.-H. Lee and D. G. Grier, "Holographic microscopy of holographically trapped three-dimensional structures," *Opt. Express* **15**, 1505–1512 (2007).
- [13] S.-H. Lee, Y. Roichman, G.-R. Yi, S.-H. Kim, S.-M. Yang, A. van Blaaderen, P. van Oostrum, and D. G. Grier, "Characterizing and tracking single colloidal particles with video holographic microscopy," *Opt. Express* **15**, 18275–18282 (2007).
- [14] J. Fung, K. E. Martin, R. W. Perry, D. M. Kaz, R. McGorty, and V. N. Manoharan, "Measuring translational, rotational, and vibrational dynamics in colloids with digital holographic microscopy," *Opt. Express* **19**, 8051–8065 (2011).
- [15] B. J. Krishnatreya and D. G. Grier, "Fast feature identification for holographic tracking: The orientation alignment transform," *Opt. Express* **22**, 12773–12778 (2014).
- [16] A. Wang, T. G. Dimiduk, J. Fung, S. Razavi, I. Kretzschmar, K. Chaudhary, and V. N. Manoharan, "Using the discrete dipole approximation and holographic microscopy to measure rotational dynamics of non-spherical colloidal particles," *J. Quant. Spectr. Rad. Trans.* **146**, 499–509 (2014).
- [17] J. Fung, R. W. Perry, T. G. Dimiduk, and V. N. Manoharan, "Imaging multiple colloidal particles by fitting electromagnetic scattering solutions to digital holograms," *J. Quant. Spectr. Rad. Trans.* **113**, 2482–2489 (2012).
- [18] R. W. Perry, G. N. Meng, T. G. Dimiduk, J. Fung, and V. N. Manoharan, "Real-space studies of the structure and dynamics of self-assembled colloidal clusters," *Faraday Discuss.* **159**, 211–234 (2012).
- [19] J. Fung and V. N. Manoharan, "Holographic measurements of anisotropic three-dimensional diffusion of colloidal clusters," *Phys. Rev. E* **88**, 020302 (2013).
- [20] F. C. Cheong and D. G. Grier, "Rotational and translational diffusion of copper oxide nanorods measured with holographic video microscopy," *Opt. Express* **18**, 6555–6562 (2010).
- [21] J. W. Goodman, *Introduction to Fourier Optics*, 3rd ed. (McGraw-Hill, New York, 2005).
- [22] R. K. Mueller, "Acoustic holography," *Proc. IEEE* **59**, 1319–1335 (1971).
- [23] J. Lezni and U. Franke, "Hektor," (2002), <http://juerglehni.com/works/hektor/>.
- [24] The open-source software for this instrument is available online at <http://github.com/davidgrier/acam>.
- [25] J. R. Potter, "Acoustic imaging using ambient noise: Some theory and simulation results," *J. Acoust. Soc. Am.* **95**, 21–33 (1994).